Journal of Magnetic Resonance 307 (2019) 106569

Contents lists available at ScienceDirect

Journal of Magnetic Resonance

journal homepage: www.elsevier.com/locate/jmr

On the influence of rotational motion on MRI velocimetry of granular flows – Theoretical predictions and comparison to experimental data

Daniel A. Clarke [a], Hilary T. Fabich [b,c], Timothy I. Brox [d], Petrik Galvosas [d], Daniel J. Holland [a,*]

[a] Department of Chemical and Process Engineering, University of Canterbury, Private Bag 4800, Christchurch 8140, New Zealand
[b] ABQMR Incorporated, Albuquerque, NM, United States of America
[c] Department of Chemical Engineering and Biotechnology, University of Cambridge, Cambridge University West Site, Philippa Fawcett Dr, Cambridge CB3 0AS, United Kingdom
[d] School of Chemical and Physical Sciences, Victoria University of Wellington, PO Box 600, Wellington 6140, New Zealand

ARTICLE INFO

Article history:
Received 6 June 2019
Revised 7 August 2019
Accepted 7 August 2019
Available online 10 August 2019

Keywords:
Granular flow
Pulsed field gradient
Magnetic resonance imaging
Velocimetry
Discrete element method
Rotational motion

ABSTRACT

Continuum dynamics of granular materials are known to be influenced by rotational, as well as translational, motion. Few experimental techniques exist that are sensitive to rotational motion. Here we demonstrate that MRI is sensitive to the rotation of granules and that we can quantify its effect on the MRI signal. In order to demonstrate the importance of rotational motion, we perform discrete element method (DEM) simulations of spherical particles inside a Couette shear cell. The variance of the velocity distribution was determined from DEM data using two approaches. (1) Direct averaging of the individual particle velocities. (2) Numerical simulation of the pulsed field gradient (PFG) MRI signal acquisition based on the DEM data. Rotational motion is found to be a significant effect, typically contributing up to 50% of the signal attenuation, thus amplifying the calculated velocity variance. A theoretical model was derived to relate an MRI signal to the angular velocity distribution. This model for the signal was compared to previously published experimental data as well as simulated MRI results and found to be consistent.

1. Introduction

Granular materials demonstrate complicated, scale dependent flow behaviour that is difficult to predict. Depending on the local flow conditions, granular material may behave analogously to solid, liquid and gaseous states of matter. There has been some success in describing granular flows using local rheological models [1]. However, granular flows are also known to exhibit non-local [2,3] flow characteristics that arise from the finite size of the grains. The non-local rheology has been linked to the velocity fluctuations of individual granules [3–5] and/or rotational motion of particles [6,7]. Detailed experimental measurements of the granular flow dynamics are required to aid the development of these non-local rheology models. Optical measurements of the dynamics are challenging owing to the opacity of granular flow. Here a magnetic resonance imaging approach is investigated to measure the granular flow dynamics, including velocity fluctuations and rotational motion. The key advance of this work over previous approaches is to develop a model to describe the effects of particle rotation on the measured signal.

When considering continuum descriptions of granular flow, it is conventional to use a Reynolds decomposition of the particle velocity $\boldsymbol{v}_p$; that is $\boldsymbol{v}_p$ is expressed as the sum of the mean $\boldsymbol{v}$, and fluctuation $\boldsymbol{u}$, of the velocity:

$$\boldsymbol{v}_p = \boldsymbol{v} + \boldsymbol{u}. \tag{1}$$

Measurement techniques to probe the velocity distribution for granular flows include using acoustic shot noise [8], particle image velocimetry [9], diffusing wave spectroscopy [10] and speckle visibility spectroscopy [11]. However, these techniques are limited to observations in the near wall region or surface of the particles. Particle tracking techniques [12–14] are not restricted to surface observations; though observations are typically restricted to the use of a single tracer particle and thus do not directly probe the entire ensemble. Furthermore, only magnetic particle tracking is able to measure rotational motion [15]. Magnetic resonance imaging (MRI) is a promising alternative technique that can measure the entire ensemble inside optically opaque systems. For granular flows, MRI has been used to measure the diffusion coefficient, correlation time, voidage [16], particle phase velocity [17] and velocity variance [18] in systems such as rotating drums, vibro-fluidised beds [19], gas fluidised beds [20] and Couette shear cells [21,22]. The effect of rotation of the particles in an ordered system was

* Corresponding author.
E-mail address: daniel.holland@canterbury.ac.nz (D.J. Holland).

https://doi.org/10.1016/j.jmr.2019.106569
1090-7807/

studied using time-of-flight MRI [21]. For an ordered system where granules form concentric layers, it is expected that the shear rate is zero within the particle and non-zero only at the interfaces between layers. This staircase velocity profile is disrupted by disordering and rotation. Optical velocimetry (which does not measure rotation) found that disordering alone was insufficient to explain the non-zero shear rate within the layers seen using MRI. From the difference between the optical and MRI shear profiles, the mean angular velocity in each of the layers was estimated. This approach is limited to highly ordered systems and does not consider the variance of the angular velocity distribution.

One challenge when developing a new MRI measurement is the validation of the measurement. The physics of MRI is well understood and can be applied to many problems, however the effect of factors such as velocity, acceleration and encoding time can be difficult to predict. Simulations of the signal acquisition with MRI are sometimes used to assist with quantifying these higher-level effects. The discrete-time solution of the Bloch equations [23] allows prediction of the spin magnetisation which is used to obtain the complex signal from which the image is generated. Furthermore, the transport of spin-bearing particles due to flow can be taken into account during the image reconstruction [24]. Here the discrete element method (DEM) is used to generate a simulated particle flow field. The particle velocities and rotational velocities are extracted directly from the simulation. Furthermore, the particle positions and rotational motion are used to confirm the model of the signal developed in this paper.

In DEM, Newton's second law of motion is numerically integrated with respect to time for each particle individually [25]. DEM simulations have been used to characterise a variety of granular flows, including annular Couette shear cells [26], rotating kilns [27,28], and hoppers [29]. DEM simulations are used to explore the fundamentals of granular flow in different flow regimes [30,31], to characterise the rheology of the bulk material [1,32,33], and to investigate fluid-particle interaction [34,35]. MRI has previously been used to validate DEM simulations of granular flow by measuring the voidage, velocity, and velocity fluctuations [36,37]. DEM has also been used to investigate MRI measurements by solving the discrete-time Bloch equations (ignoring relaxation) using particle position information from DEM [38]. These simulations were able to confirm that the mean velocity obtained from experiments is equivalent to a particle-weighted time-averaged velocity. However, in that work, fluctuations in the particles' velocities were not considered. Furthermore, particles were approximated as point masses and so the effects of rotation could not be modelled.

This article presents a detailed investigation of pulsed-field-gradient (PFG) MRI measurements of the fluctuating component of the particles' motion, including the effect of rotation. A theoretical model of the signal is developed to describe the effect of rotation of granules on the MRI signal. The model is tested using both simulated and experimental data. A schematic of the studied systems and analytical techniques presented in this article is shown in Fig. 1. Simulated MRI signals are obtained by solving the discrete-time Bloch equations using DEM simulations of particles in a Couette cell under annular shear, as shown by the branch "Bloch equation simulation" in Fig. 1. The outputs of the simulation are used for two purposes: First, the DEM outputs (positions, velocities and rotational velocities for each particle) are directly averaged to obtain, at any spatial position, the true mean velocity, velocity variance and rotational velocity variance. We refer to these as numerical directly averaged values, as presented by the branch "Direct averaging" in Fig. 1. Second, the model of the signal is validated by calculating the angular velocity variance from the simulated MRI signal (shown as the "Fit model to signal" block in Fig. 1) and comparing it with the directly averaged angular velocity variance. The MRI simulations are then compared with previously reported experimental MRI measurements of granular motion [22], shown in the branch "Physical MRI experiment" in Fig. 1.

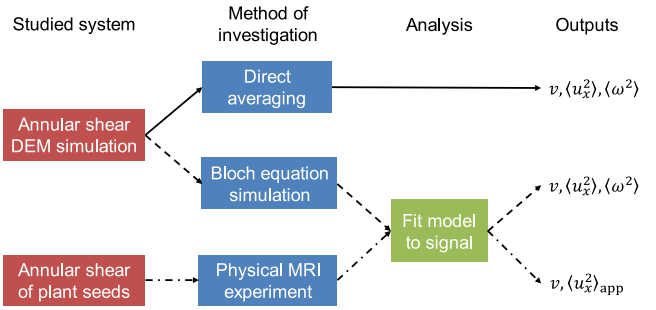

Fig. 1. Illustration of the systems studied, methods of investigation, analysis and outputs. The outputs from DEM simulations of annular shear flow are obtained by (1) direct averaging, and (2) simulating the acquisition of the MRI signal by solving the discrete-time Bloch equations, followed by fitting the model signal equation to the simulated signal. Physical annular shear experiments using plant seeds were measured using MRI as reported in [22] and analysed using the model signal equation.

2. Theory

2.1. Conventional analysis

PFG experiments can be used to measure the velocity distribution of fluids or particles [39]. Here these are briefly reviewed, before the analysis is extended to include the effects of rotation. The phase shift of a spin (i.e. the phase acquired in a reference coordinate system rotating with the Larmor frequency $\omega = \gamma B_0$) is the integral of the strength of the magnetic field gradient and the position of the spin, $\boldsymbol{x}$, with respect to time:

$$\theta(t) = \gamma \int_0^t \boldsymbol{g}(t') \cdot \boldsymbol{x}(t') dt', \tag{2}$$

where γ is the gyromagnetic ratio and the gradient is denoted by $\boldsymbol{g}(t')$. For the granular systems studied here, the particles contain mobile oil which enables signal to be detected. The particle position is decomposed into an initial position, $\boldsymbol{x}_0$, local mean velocity $\boldsymbol{v}$ and spatial fluctuation about the mean velocity $\boldsymbol{u}$ giving:

$$\theta = \gamma \int \boldsymbol{g}(t) t \cdot (\boldsymbol{v} + \boldsymbol{u}) dt + \gamma \boldsymbol{x}_0 \cdot \int \boldsymbol{g}(t) dt \tag{3}$$

For PFG measurements, bipolar gradients separated by a time, Δ, are applied such that the integral $\int \boldsymbol{g}(t) dt$ is equal to zero. Analogous to the concept of k-space for spin density imaging, an inverse variable known as $\boldsymbol{p}$ is defined by $\boldsymbol{p} = \gamma \int \boldsymbol{g}(t) t dt$. If acceleration and higher derivatives of position are ignored, the signal within a finite volume element such as an image voxel is then defined as:

$$S(\boldsymbol{p}) = \int \rho(\boldsymbol{x}) \exp(i\boldsymbol{p} \cdot (\boldsymbol{v} + \boldsymbol{u})) dV \tag{4}$$

where $\rho(\boldsymbol{x})$ is the spin density at position $\boldsymbol{x}$. The gradient is chosen such that the motion is encoded along the x-axis only. Since the measurement is along x, only the components v_x, u_x and p_x need to be considered. If we assume each particle contributes the same signal, then by defining the velocity distribution of the particles within the volume element as $P(u_x)$, the integral may be expressed as:

$$S(p_x) = \int P(u_x) \exp(i p_{\boldsymbol{x}}(v_x + u_x)) du_x \tag{5}$$

Given that the mean velocity is constant and assuming that the velocity distribution along x is Gaussian, Eq. (5) is integrated with respect to u_x to yield:

$$S(p_x) = \frac{1}{\sqrt{\langle u_x^2\rangle 2\pi}} \exp(ip_x v_x) \exp\left(-\frac{1}{2}p_x^2\langle u_x^2\rangle\right). \quad (6)$$

The signal for when the gradient (and hence p_x) is equal to zero is denoted as S_0, and is used to normalise the signal. Thus, the phase of the normalised signal provides information about the mean velocity v_x, whereas the absolute value of the normalised signal gives the variance of velocity:

$$\left|\frac{S}{S_0}\right| = \exp\left(-\frac{1}{2}p_x^2\langle u_x^2\rangle\right) \approx 1 - \frac{1}{2}p_x^2\langle u_x^2\rangle. \quad (7)$$

Hence, at low values of p_x, the normalised signal is described by a quadratic with respect to p_x, with the velocity variance given by the coefficient of p_x^2.

2.2. Effect of rotation

Particle rotation is not normally considered in MRI, however it also contributes to the signal attenuation since the spins on a rotating particle will travel with different velocities. We define a Cartesian coordinate system x, y, z, where the flow encoding axis is along the x-axis and the origin is located at the particle centre of mass. Therefore, we consider only rotation along the y and z axes, the angular velocity about these axes are denoted by ω_y and ω_z. Rotation about x does not affect the signal. Assuming that $\omega\Delta$ is sufficiently small (<0.5 rad [40]), it is reasonable to assume the projection of the rotational velocity along the (linear) velocity encoding axis is constant during the period Δ. Thus, the signal from a particle has a general form given by:

$$S = \iiint \rho(x,y,z) \exp(ip_x(v_x + u_x + z\omega_y + y\omega_z))dV_p, \quad (8)$$

where it is assumed that the spin density ρ is uniform and of arbitrary value. The variable of integration, V_p, is the volume enclosed by the particle surface. For simplicity, ρ is assumed to be unity, and hence may be ignored.

For bipolar gradient pulses, the signal does not depend on the initial position of the particle. Therefore, the total signal from a region of interest containing many particles is equal to:

$$S = \sum_i \iiint \exp(ip_x(v_{x,i} + u_{x,i} + z\omega_{y,i} + y\omega_{z,i}))dV_{p,i}, \quad (9)$$

where the summation is over all particles i in a specified region. The translational velocity components are uniform over V_p, thus the v_x and u_x terms are shifted out of the integral over the particle. A change of variables is then performed, where the summation is replaced by the probability distribution for the velocities of the particles $f(\omega_y, \omega_z, u_x)$:

$$S = \iiint f(\omega_y,\omega_z,u_x) \exp(ip_x(v_x+u_x)) \times \iiint \exp(ip_x(z\omega_y + y\omega_z))dV_p d\omega_y d\omega_z du_x. \quad (10)$$

It was assumed that the distributions of the translational and angular velocities were independent, i.e. $f(\omega_y,\omega_z,u_x) = P(\omega_y)P(\omega_z)P(u_x)$, where $P(\omega_y)$ and $P(\omega_z)$ are the angular velocity distributions about axes y and z, respectively. The assumption of independent velocity distributions implies that the angular velocity components of each particle are uncorrelated. It was further assumed that $P(\omega_y)$ and $P(\omega_z)$ are Gaussian distributed, with a mean of zero and the variance denoted by $\langle\omega_y^2\rangle$ and $\langle\omega_z^2\rangle$. The mean velocity term is taken outside the integral and the integration is performed with respect to u_x, as described in the previous section. Thus, the signal takes the form:

$$S(p_x) = \frac{\exp(ip_x v_x)\exp\left(-\frac{p_x^2}{2}\langle u_x^2\rangle\right)}{\sqrt{\langle u_x^2\rangle 2\pi}} \times \int P(\omega_y)\int P(\omega_z)\iiint \exp(ip_x(z\omega_y + y\omega_z))dV_p d\omega_y d\omega_z. \quad (11)$$

The integration is simplified by approximating the exponential terms as Taylor series expansions. These series are expressed as the Cauchy product and the resulting volume integral is solved using a set of reduction formulae. These aspects of the derivation are described in more detail in Appendix A. Normalisation of the signal at $p_x = 0$ gives:

$$\frac{S}{S_0} = \exp(ip_x v_x)\exp\left(-\frac{p_x^2}{2}\langle u_x^2\rangle\right) \times \sum_{m=0}^{\infty}\sum_{l=0}^{m} \frac{i^m(l-1)!!(m-l-1)!!}{c_{0,0}l!(m-l)!} p_x^m c_{l,m-l} R^m \langle\omega_y^2\rangle^{l/2}\langle\omega_z^2\rangle^{(m-l)/2}. \quad (12)$$

where $c_{l,m-l}$ is a coefficient associated with the recursive integral and R is the particle radius. It is of interest to obtain the angular velocity variance in terms of the signal, hence the series is truncated at $m = 2$. For consistency, the exponential that represents the translational velocity variance term is also approximated by a truncated Taylor series. The terms $\langle\omega_y^2\rangle$ and $\langle\omega_z^2\rangle$ in Eq. (12) cannot be determined independently, thus, it is assumed that the system is isotropic, i.e. $\langle\omega_y^2\rangle = \langle\omega_z^2\rangle = \langle\omega^2\rangle$. Rewriting Eq. (12) with these changes yields:

$$\frac{S}{S_0} = \exp(ip_x v_x)\left(1 - \frac{p_x^2}{2}\langle u_x^2\rangle\right)\left(1 - \frac{1}{5}p_x^2R^2\langle\omega^2\rangle\right). \quad (13)$$

Hence, granule rotation contributes towards signal attenuation, whereas signal attenuation has previously been solely attributed to translational fluctuations in the standard analysis method. The rotational component of the signal may be expressed in terms of an apparent translational velocity variance, $\langle u_x^2\rangle_\omega$, analogous to Eq. (7). This apparent translational velocity variance is related to the angular velocity variance by:

$$\langle u_x^2\rangle_\omega = \frac{2}{5}R^2\langle\omega^2\rangle. \quad (14)$$

Eq. (14) provides a basis to compare the magnitude of angular velocity fluctuations with the translational velocity fluctuations for a generic region of interest. The flow encoding sequence can be coupled with imaging to spatially localise measurements into voxels. In this paper, we refer to Eq. (12) as the theoretical signal model and Eq. (13) as the truncated signal model. Comparisons with both the complete theoretical model and the truncated model will be performed.

3. Method

3.1. MRI experiment

The experiments used in this work are those of Fabich et al. [22], performed on a concentric cylinder rheo-NMR device. A complete description of the experimental measurements is already published; here only a brief summary of the key parameters is included. The Couette cell consisted of a stationary outer cylinder with diameter of 47.3 mm and a rotating inner cylinder whose dimension could be changed to control the gap size between the inner and outer wall. Particles were placed in the gap between

the inner and outer cylinder. The base of the outer cylinder was fixed and the top of the bed was free to expand or contract. Particles were fixed to the walls of the cylinder to minimise slip and prevent solid body rotation. Experiments were performed with particles of different diameters and gap sizes. Here the experiments using 0.44 mm, and 0.60 mm diameter particles with a gap size of 7.65 mm were used. Experiments were performed with inner wall velocities U of 17 mm s^{-1} and 41 mm s^{-1}. The velocity distribution was measured using a double slice-selective, PFG spin echo measurement. Flow encoding was spatially resolved in the y-direction across the Couette cell with a 65 mm field-of-view and a resolution of 127 μm per pixel. Velocity was encoded in the x-direction, i.e. perpendicular to the direction of spatial encoding. The vertical slice was 10 mm, and a horizontal slice of 1 mm was used to ensure that the curvature of the sample does not have a significant effect on the motion measured, hence providing a mapping $v_x = v_\theta$ of the Cartesian to cylindrical velocity components [41]. The flow encoding gradients were applied for a duration δ = 1 ms, with an observation time Δ = 3 ms. The choice of observation time may affect the measured velocity distribution due to collisions between granules. If Δ is below the mean collision time, then the velocity variance is expected to be independent of Δ [18]. For the experimental system, the velocity variance was insensitive to values of Δ between 3 and 4 ms [22], hence data collected using an observation time within this range is suitable for comparison.

3.2. Simulation details

The DEM simulations were performed in the open-source software LIGGGHTS. The full details of this programme are given by Kloss et al. [42]. In brief, Newton's equations of motion are numerically solved for each particle. Collisions between particles were resolved using the Hertzian soft-sphere contact force scheme.

The Couette cell, shown in Fig. 2, had an outer diameter of 47.3 mm and an inner diameter of 32 mm, corresponding to the experimental geometry. To replicate the seeds being glued to the side walls of the cell in the experimental setup, single cylindrical layers of particles were placed next to the walls. The particle arrangement was face-centred, touching along the diagonals, with horizontal and vertical spacing equal to $\sqrt{8}R$. For the inner wall, the particle velocity components were set to match the linear velocity of the rotating cylinder. At the outer wall, the particle velocity components were set to zero. The system was initialised by simulating 40,000 particles being poured into the annular gap. The particles were 0.44 or 0.60 mm diameter spheres. The system was sheared for 3 s. The rotational velocity of the inner cylinder was set to 17 mm s^{-1} or 41 mm s^{-1}.

The Poisson ratio was set to 0.33, and the restitution coefficient e_n was 0.9. The static friction coefficient μ_f was tested at values of 0.1 and 0.5. The elastic modulus for the particles was set to 1×10^7 Pa in order to ensure that the computational time required was suitably low. The time step Δt was fixed at 1×10^{-6} s. Time steps are advised to be below 25% of the Rayleigh time for numerical stability [43]. The time step used here was 8% of the Rayleigh time for the 0.44 mm particles with the given contact parameters and 6% for the 0.60 mm particles. Thus, this time step was deemed to be sufficiently low. The velocity Verlet scheme was used to solve the equations of motion for the particle positions and velocities over time.

To compare DEM data to MRI, the discrete particle data were converted into continuum variables by direct averaging. Direct averaging involves binning DEM particle velocity data into voxels according to the positions of particles, followed by calculation of the local mean and variance of the binned particles' velocity. MRI measurements of velocity variance differ from the directly averaged variance by the following: (1) flow encoding occurs over a finite time, Δ; (2) MRI gives time-averaged values of the mean and variance of the velocity; (3) the finite observation time Δ means that the displacement of nuclear spins due to particle rotation also contributes to the MRI signal. In the supplementary material, we investigate the significance of the effects of acquisition and time averaging by comparing different mathematical definitions for the mean velocity and velocity variance. Here, we use the definition that was found to most closely correspond to that recovered from MRI (Method 4 in the supplementary material). First, the velocity of particle p for sampling i is calculated as an average over the flow encoding time Δ:

$$v_{x,p,i} = \frac{x_p\big|_{t=t_i+\delta+\Delta} - x_p\big|_{t=t_i}}{\delta + \Delta}. \tag{15}$$

The local mean velocity is then obtained by averaging these individual velocity values over N_p particles and N_s sampling times (or repetitions) according to:

$$v_x = \frac{\sum_{i=1}^{N_s}\sum_{p=1}^{N_p} v_{p,x,i}\phi_{p,i}}{\sum_{t=1}^{N_s}\sum_{p=1}^{N_p}\phi_{p,i}}. \tag{16}$$

The velocity variance is then obtained from:

$$\langle u_x^2 \rangle = \frac{\sum_{i=1}^{N_s}\sum_{p=1}^{N_p}\left(v_{x,p,i} - v_x\right)^2\phi_{p,i}}{\sum_{i=1}^{N_s}\sum_{p=1}^{N_p}\phi_{p,i}}, \tag{17}$$

where $\phi_{p,i}$ is the volume fraction of particle p at sampling i that resides within each voxel. The rectangular region of interest (ROI) shown in Fig. 2 was divided into a series of voxels along the y-axis. The ROI was 1 mm high by 1 mm wide. This region is analogous to the region selected experimentally using the double slice selective pulses. Here, the vertical dimension was smaller than used in the experiment due to the small size of the computational domain used. The system varies only slightly along the vertical direction hence the reduced size of the domain in the vertical direction does not influence the results. The particle volume fraction in

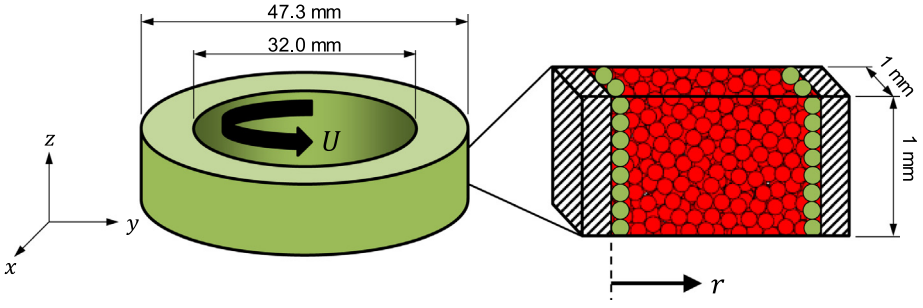

Fig. 2. Diagram of the annular Couette flow system simulated by DEM. Data from the inset were used for post-processing.

each voxel at the end of flow encoding was calculated by the correlation from Khawaja et al. [44], which has previously been found to give accurate volume fractions and a low computation time [45]. Time-averaged profiles were then obtained by taking the average over 30 samples collected at 0.1 s time intervals. Data from both sides of the Couette were averaged, producing profiles of mean velocity and velocity variance against distance from the inner wall.

3.3. Algorithm for simulated MRI signal acquisition

Simulating the MRI experiments enabled the effect of rotation on the signal to be quantified. The signal was simulated using: (1) translational motion only, (2) rotational motion only, and (3) both translation and rotation. Differences in the mean and variance profiles of the velocity between these three sets of results may be attributed to particle rotation. Each particle was represented as a collection of 3500 satellite points surrounding the centroid of the particle. The centre position of each particle was updated at each step by first-order numerical integration of the translational velocity obtained from the DEM simulation as a function of time. The difference between numerical integration of the velocity data and the DEM positions was negligible. The interval between steps was 0.1 ms. The angular velocity component of each particle was used to calculate the rotation matrix for each satellite point. The updated linear position of each satellite point $\boldsymbol{x}'$ due to rotation was calculated by generating a rotation matrix from the angular velocities, and multiplying this rotation matrix by the pre-rotation position $\boldsymbol{x}$ of the satellite point relative to the particle centre, as shown by:

$$\boldsymbol{x}' = \begin{bmatrix} 1 & 0 & 0 \\ 0 & \cos\theta_x & -\sin\theta_x \\ 0 & \sin\theta_x & \cos\theta_x \end{bmatrix} \begin{bmatrix} \cos\theta_y & 0 & \sin\theta_y \\ 0 & 1 & 0 \\ -\sin\theta_y & 0 & \cos\theta_y \end{bmatrix} \times \begin{bmatrix} \cos\theta_z & -\sin\theta_z & 0 \\ \sin\theta_z & \cos\theta_z & 0 \\ 0 & 0 & 1 \end{bmatrix} \boldsymbol{x}, \tag{18}$$

where $\theta_i = \omega_i \Delta t$. Note that the DEM simulations consider rotations about all three axes, as do the discrete-time solutions to the Bloch equations. Thus, these simulations serve to check the assumption that rotation about x may be ignored in our theoretical model of the signal. The DEM data were output at 100 μs intervals to minimise data storage requirements. These data were output for 4.5 ms, which corresponds to the flow encoding time in the MRI experiments. In order to replicate the longer total experiment time of the MRI, these 4.5 ms sample periods were repeated at intervals of 0.1 s, which corresponds to a displacement of at least 1 d_p for most of the particles in the bed. For each DEM simulation, a total of 30 flow encoding samples were obtained where for each sample, the positions were recorded for 4.5 ms and the ROI contained approximately 1000 particles. The simulated MRI pulse sequence is shown in Fig. 3.

A square-wave gradient was applied for a half-period (δ) of 1 ms. The observation time between gradients (Δ) was 3.5 ms. The amplitude of the gradient was adjusted in 64 steps about 0 T m^{-1}, with a maximum gradient strength equal to 0.34 T m^{-1}.

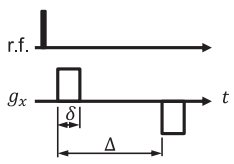

Fig. 3. Diagram of the simulated MR sequence used to measure the mean velocity and the granular temperature in the DEM simulations of Couette flow.

The phase of each satellite point was calculated by first order numerical integration of $\gamma \boldsymbol{g}(t) \cdot \boldsymbol{x}(t)$ with respect to time. The phase of each satellite point was then converted into a complex signal. These signals were allocated to bins according to the position of the satellite points at the end of the sampling period ($\Delta + \delta$). The signals were summed together to give the total signal within the voxel. The simulated signals are processed in the same manner as the experimental signals to extract the mean velocity and the variance of the velocity distribution. The mean velocity was calculated using:

$$v_x = \frac{\arg(S/S_0)}{p_x}. \tag{19}$$

According to Eq. (7), the variance of the velocity is found by fitting a second-order polynomial to the translational motion component of normalised signal against p_x. The variance is the second-order fitting coefficient. Considering rotation, the variances are found by fitting a second-order polynomial to the rotational component of the normalised signal against p_x as shown in Eq. (13).

4. Results and discussion

In this section, we first compare the theoretical model of the signal shown by Eq. (12) to MRI simulations of an idealised test case where the translational and angular velocities are independent. Next, the truncated model of the signal shown by Eq. (13) is used to calculate the translational and angular velocity variances of the MRI simulation of DEM annular shear flow, which are then validated against the physical MRI experiments reported in [22].

4.1. Verification of the theoretical model of the signal

In this section, the theoretical model of the signal developed in Section 2 is verified. The prediction from Eq. (12) was compared with the simulated MRI signal from the trajectories of 10,000 non-interacting particles. The particles are non-interacting such that there is no change in the velocity during flow encoding. Thus, this scenario represents an idealised case to test the theoretical signal model. The motion encoding gradient was defined as being along the x-axis, and the gradient strength, observation time and encoding time were set as defined in Section 3.3. Gaussian translational and angular velocity distributions were imposed on the system. In all cases, the mean translational and angular velocities of the system were set to zero. In these simulations, the translational and both angular velocity components were uncorrelated and randomly sampled from distributions with variances $\langle u_x^2 \rangle$, $\langle \omega_y^2 \rangle$ and $\langle \omega_z^2 \rangle$, respectively. First, the variance of the angular velocity distributions about each axis were set to be identical, i.e. isotropic. Fig. 4 (a) shows the absolute value of the normalised signal against the angular velocity variance for several translational velocity variances. Irrespective of the translational velocity variance, excellent agreement between the simulations and model was observed, demonstrating that the theoretical model was able to describe the effects of translational and rotational motion on the signal when these components were independent. Fig. 4(b) demonstrates that the model predictions agree well with the MRI simulation, even at the maximum values of $|p_x|$ that were measured experimentally ($p_x = 400$ s mm^{-1}). An example of correlated rotational velocities is shown (blue crosses), where the agreement between simulations and Eq. (12) is poor since the assumption of independent velocity distributions was violated. These results confirm the validity of the theoretical model, provided the assumption of independent velocity distributions is valid.

The theoretical signal model does not assume that the system is isotropic. It should, in principle, also be applicable for anisotropic

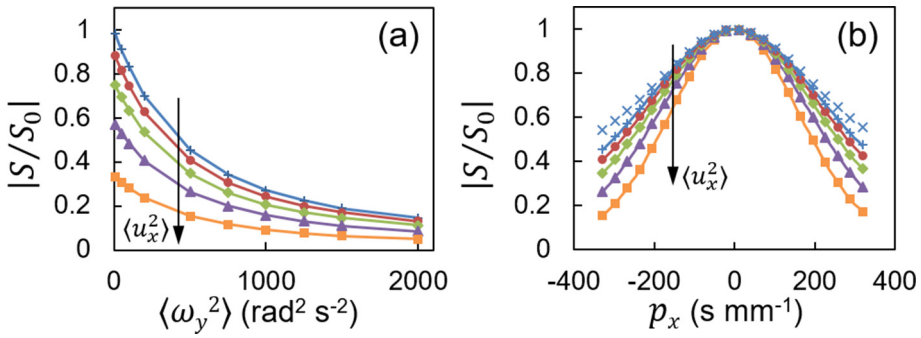

Fig. 4. MRI simulations of a generated set of particles with Gaussian translational and angular velocity distributions. (a) Normalised signal against angular velocity variance where $p_x = -330$ s mm^{-1}, $\langle \omega_z^2 \rangle = \langle \omega_y^2 \rangle$. (b) Normalised signal against p where $\langle \omega_y^2 \rangle = \langle \omega_z^2 \rangle = 500$ rad^2 s^{-2} MRI simulation data are denoted by markers, Eq. (12) is denoted by solid lines of the corresponding colours. $\langle u_x^2 \rangle = 0$ mm^2 s^{-2} (+), $\langle u_x^2 \rangle = 2$ mm^2 s^{-2} (●) $\langle u_x^2 \rangle = 5$ mm^2 s^{-2} (♦), $\langle u_x^2 \rangle = 10$ mm^2 s^{-2} (▲), $\langle u_x^2 \rangle = 20$ mm^2 s^{-2} (■). A special case where $\langle u_x^2 \rangle = 0$ and the angular velocity components of the granules are correlated (i.e. $\omega_y = \omega_z$) is also shown (×). (For interpretation of the references to colour in this figure legend, the reader is referred to the web version of this article.)

systems. To verify the model for anisotropy, the simulation described in the preceding paragraph was repeated with anisotropic rotational components by sampling ω_y and ω_z from distributions with variances $\langle \omega_y^2 \rangle$, and $\langle \omega_z^2 \rangle$, respectively, i.e. $\langle \omega_y^2 \rangle \neq \langle \omega_z^2 \rangle$. Fig. 5(a) gives the signal attenuation with respect to the velocity variances about the y and z axes for the MRI simulation and the theoretical signal model when the velocity variance was zero. Fig. 5(b) shows the relationship between the signal and the inverse variable p_x for several combinations of the angular velocity variances. Agreement between the simulations and the model is excellent.

In Fig. 5(b) and (b), at low p_x the signal follows an approximately parabolic shape, but at higher p_x there is an inflection in the signal intensity such that it is no longer parabolic in shape. Therefore, back-calculation of the variance with the truncated signal model of Eq. (13), which is parabolic, may not always provide an accurate estimate of the velocity variance. We explore the suitability of this method in the following section.

4.2. Couette flow verification and validation

Simulations permit easy isolation of rotational and translational motion effects on the signal. The inverse function of the truncated signal model of Eq. (13) was used to calculate the contribution of translational and angular velocity variances for granular Couette flow. First, only the translational velocities are considered. The mean velocity and the variance of the translational velocity were calculated by direct averaging as described by Eqs. (16) and (17), respectively. In Fig. 6, Eq. (12) was compared against the signal

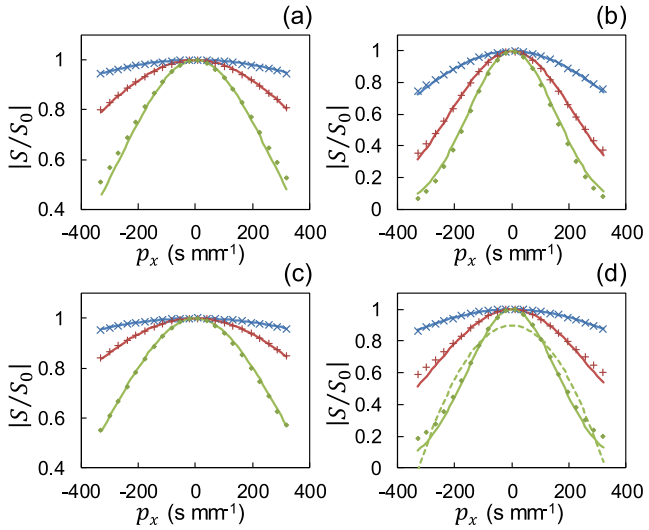

Fig. 6. Profiles of the absolute normalised signal from translational motion against the inverse variable for granular Couette flow of 0.44 mm particles (a) $U = 17$ mm s^{-1}, $\mu_f = 0.1$, (b) $U = 41$ mm s^{-1}, $\mu_f = 0.1$, (c) $U = 17$ mm s^{-1}, $\mu_f = 0.5$, (d) $U = 41$ mm s^{-1}, $\mu_f = 0.5$. MRI simulation data are denoted by markers. The result from Eq. (12) was calculated by extracting the rotational and translational variances from the DEM data using direct averages and are denoted by solid lines. In (d), the fit of Eq. (13) to the simulated MRI data is shown by the green dashed line. Profiles at $r = 1.5$ mm (♦), $r = 2.1$ mm (+), and $r = 2.6$ mm (×). (For interpretation of the references to colour in this figure legend, the reader is referred to the web version of this article.)

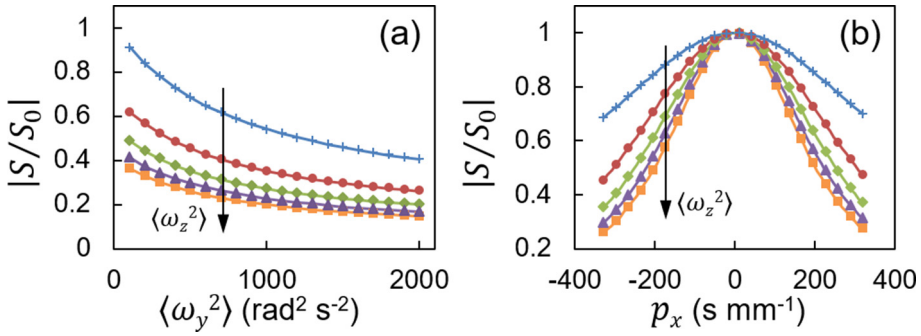

Fig. 5. MRI simulations of a generated set of particles with Gaussian translational and angular velocity distributions. (a) Normalised signal against angular velocity variance about the y-axis for constant values of angular velocity about the z-axis for $\langle u_x^2 \rangle = 0$ and $p_x = -330$ s mm^{-1}. (b) Normalised signal against p_x where $\langle u_x^2 \rangle = 0$ and $\langle \omega_z^2 \rangle = 500$ rad^2 s^{-2}. MRI simulation data are denoted by markers, Eq. (12), where $m = 40$ is denoted by solid lines. $\langle \omega_y^2 \rangle = 0$ rad^2 s^{-2} (+), $\langle \omega_y^2 \rangle = 500$ rad^2 s^{-2} (●), $\langle \omega_y^2 \rangle = 1000$ rad^2 s^{-2} (♦), $\langle \omega_y^2 \rangle = 1500$ rad^2 s^{-2} (▲), $\langle \omega_y^2 \rangle = 2000$ rad^2 s^{-2} (■).

predicted using the MRI simulation of translational motion for the 0.44 mm particles. Similar profiles were found for the simulations involving 0.60 mm diameter particles (not shown here). At the inner moving wall i.e. $r < d_p$, the agreement is poor (not shown) since the granules have identical velocities, which violated the assumption of Gaussian-distributed velocities. Beyond the moving wall, the agreement between Eq. (12) and the MRI simulation of the DEM particle trajectories was generally very good. However, in cases where the angular velocity variance is particularly high, for example Fig. 6(d) where $\mu_f = 0.5$ and $U = 41$ mm s^{-1}, significant deviations occur for greater values of p_x. These localised deviations suggest that obtaining the most accurate value for the variance requires fitting to a subset of the data at low p_x, analogous to the measurement of flow propagators in porous media [46].

In order to compare the effects of rotation and translation, it is useful to fit the truncated signal model (Eq. (13)) over a range of p_x that avoids the inflection point at high p_x. In Fig. 6(d), the truncated signal model fitted to the simulated MRI signal data is shown by the dashed line. The fitted model deviates visibly from the simulated MRI signal as a result of including the inflected data in the fit. To quantify what constitutes an acceptable range of p_x, Fig. 7 shows the fitted variance in terms of the maximum p_x used in the fit. The resulting variances are compared to the direct average. The standard error in the direct average assuming that the velocity is normally distributed was calculated by [47]:

$$\Delta\langle u_x^2\rangle = \sqrt{\frac{2\langle u_x^2\rangle}{N_p - 1}}. \tag{20}$$

For these cases, the value of the variance is not sensitive to the fitting range for small p_x, i.e. here $p_x < 100$ s mm^{-1}. When fitted over the maximum p_x tested, a growing deviation from the low-p_x fit is observed. This deviation occurs due to the signal departing from the parabolic form assumed by Eq. (13). The deviation is strongest at the highest variances tested (about 40 mm^2 s^{-2}). For these systems, the signal flattens out as it is nearly completely attenuated. The agreement between the variance fitted to the MRI simulations and the direct averages (shown by the solid lines) is very good for low p_x, with deviations below 10% and

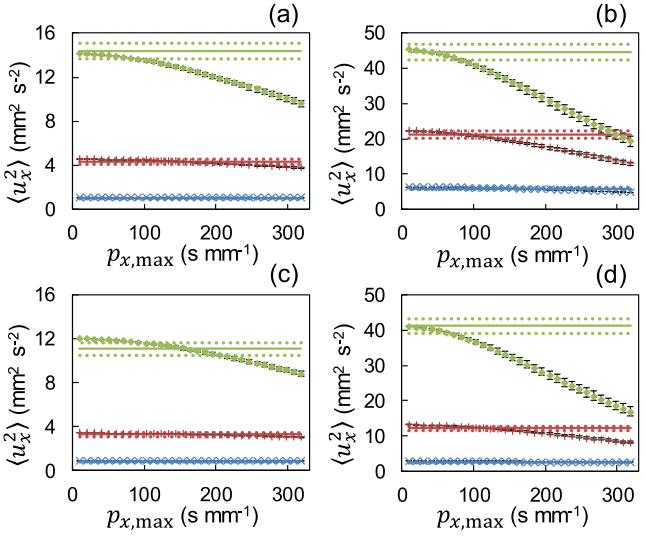

Fig. 7. The translational velocity variance measured by fit of Eq. (7) to MRI simulations as a function of the fitting range for granular Couette flow of 0.44 mm particles. (a) $U = 17$ mm s^{-1}, $\mu_f = 0.1$, (b) $U = 41$ mm s^{-1}, $\mu_f = 0.1$, (c) $U = 17$ mm s^{-1}, $\mu_f = 0.5$, (d) $U = 41$ mm s^{-1}, $\mu_f = 0.5$. Direct averages are shown by solid lines. The standard error in the direct average (Eq. (20)) is denoted by the dotted lines. Markers show the fits of Eq. (7) to MRI simulation data at $r = 1.5$ mm (♦), $r = 2.1$ mm (+), and $r = 2.6$ mm (×). The error bars represent the uncertainty in the fit to the MRI simulation data.

within the statistical error obtained from Eq. (20). Hence, if the fit of Eq. (7) to the simulated MRI signal is over a range of p_x where the fit is not sensitive to the maximum value of p_x then MRI is able to recover the time average of the observation-averaged translational velocity variance.

The suitability of PFG sequences for measuring the angular velocity variance was assessed using a similar approach to that used for the translational velocity. The angular velocity variance was calculated using a modified direct average, where the local mean angular velocity was given by:

$$\overline{\omega}_y = \frac{\sum_{i=1}^{N_s}\sum_{p=1}^{N_p}\omega_{y,p,i}\phi_{p,i}}{\sum_{i=1}^{N_s}\sum_{p=1}^{N_p}\phi_{p,i}}, \tag{21}$$

where the individual particle angular velocities from the DEM were averaged over the flow encoding time consisting of N instantaneous time points, i.e. $\omega_{y,p,i} = 1/N\sum_{t=0}^{N}\omega_{y,p,i,t}$. The angular velocity variance was calculated using:

$$\langle\omega_y^2\rangle = \frac{\sum_{i=1}^{N_s}\sum_{p=1}^{N_p}\left(\omega_{y,p,i} - \overline{\omega}_y\right)^2\phi_{p,i}}{\sum_{i=1}^{N_s}\sum_{p=1}^{N_p}\phi_{p,i}}. \tag{22}$$

These locally averaged variables were used as inputs to Eq. (12) to estimate the MR signal using our theoretical model. From this signal, the translational and angular velocity variance was calculated from the inverse function of Eq. (13).

Fig. 8 compares the MRI simulations and the theoretical signal model given by Eq. (12) against p_x. This model follows the simulated MRI signal from the DEM trajectory data well, although deviations are apparent at the highest values of p_x tested for $\mu_f = 0.5$ and $U = 41$ mm s^{-1} shown in Fig. 8(d). The effect of fitting range on the recovered angular velocity variance is related to the direct average in Fig. 9. At small fitting ranges, the recovered angular velocity variance was approximately constant, however significant deviation was observed for the widest fitting ranges at high angular velocity variances, identical to the translational motion shown in Fig. 7. The region of constant $\langle\omega^2\rangle$ was generally in good agreement with the directly averaged angular velocity variance, to within statistical uncertainty. As with the translational velocity variance, if the fit of Eq. (13) to the simulated MRI signal is limited

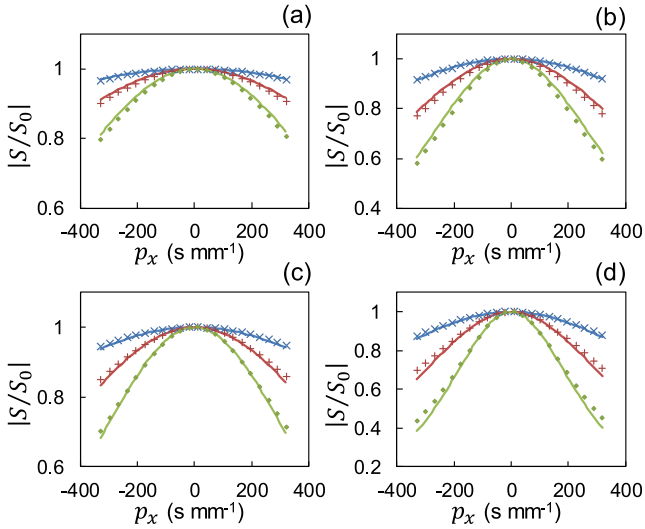

Fig. 8. Profiles of the signal from angular motion against the inverse variable for granular Couette flow of 0.44 mm particles (a) $U = 17$ mm s^{-1}, $\mu_f = 0.1$, (b) $U = 41$ mm s^{-1}, $\mu_f = 0.1$, (c) $U = 17$ mm s^{-1}, $\mu_f = 0.5$, (d) $U = 41$ mm s^{-1}, $\mu_f = 0.5$. MRI simulation data are denoted by markers, the result from Eq. (12) was calculated using direct averages and are denoted by solid lines. Profiles at $r = 1.5$ mm (♦), $r = 2.1$ mm (+), and $r = 2.6$ mm (×).

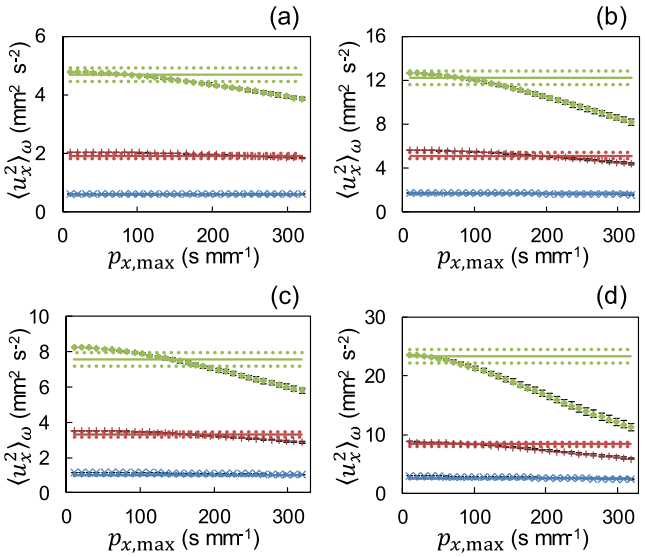

Fig. 9. The angular velocity variance measured by fit of Eq. (13) to MRI simulations as a function of the fitting range for granular Couette flow of 0.44 mm particles. (a) U = 17 mm s^{-1}, μ_f = 0.1, (b) U = 41 mm s^{-1}, μ_f = 0.1, (c) U = 17 mm s^{-1}, μ_f = 0.5, (d) U = 41 mm s^{-1}, μ_f = 0.5. Direct averages are shown by solid lines. The standard error in the direct average (Eq. (20)) is denoted by the dotted lines. Markers show the fits of Eq. (13) to MRI simulation data at r = 1.5 mm (♦), r = 2.1 mm (+), and r = 2.6 mm (×). The error bars represent the uncertainty in the fit to the MRI simulation data.

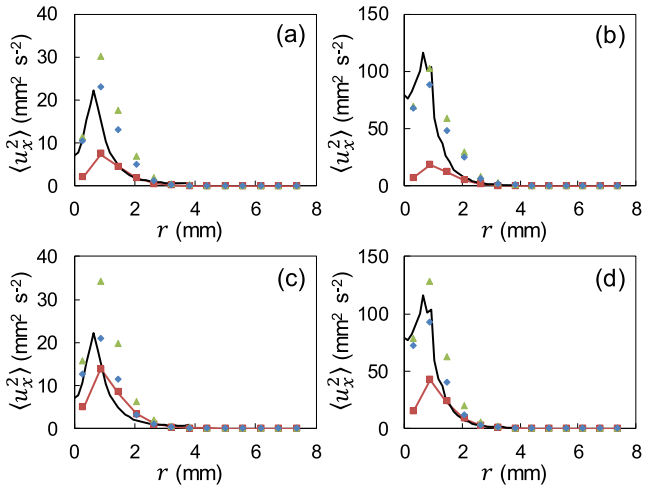

Fig. 11. Comparison of experimental and simulated velocity variance profiles of Couette shear with 0.44 mm d_p particles. The MRI experiments (▬) were reported previously [22] and were run at the same U as the simulations. DEM simulations were performed with parameters of (a) μ_f = 0.1, U = 17 mm s^{-1}, (b) μ_f = 0.1, U = 41 mm s^{-1}, (c) μ_f = 0.5, U = 17 mm s^{-1}, (d) μ_f = 0.5, U = 41 mm s^{-1}. MRI simulations incorporated translational motion only (case 1) (♦), angular motion only (case 2) (■), and both translational and angular motion (case 3) (▲). Direct averages were calculated for the translational velocity variance (▬) and angular velocity variance (▬).

to a narrow range of p_x then the time-averaged angular velocity variance can be determined using MRI.

We now compare the relative contributions of the translational and rotational motion to the attenuation of the signal. The velocity variance was found by fitting to Eq. (7) using three versions of the simulated MR signal: (1) only translational motion of the granules contributed towards the signal, (2) only particle rotation contributed to the signal, and (3) both rotation and translation of granules contributed to the signal. For (2), the apparent velocity variance obtained from the fit is related to the angular velocity variance by Eq. (14). Experimentally, the situation described in (3) occurs. MRI simulation has enabled us to produce variance profiles for (1) and (2), which are not possible to obtain from the experiments reported in [22]. Fig. 10(a) shows the signal attenuation across the gap as measured by the MRI simulation of the DEM particle trajectories for these three cases. At the inner wall, signal attenuation is low for all cases. Particles fixed to the wall have the same velocity and are not free to rotate. The signal reaches a local minimum about $\sim 1 d_p$ from the inner wall. In this rapid flowing region, granules exhibit a distribution of velocities and rotate as a result of frictional contacts. Further away from the inner wall, the signal attenuation is reduced due to the narrowing of velocity distributions as kinetic energy is dissipated. Near the outer wall, there is negligible signal attenuation since the granules are nearly static. The signal attenuation is greatest for case 3 where the effects of cases 1 and 2 occurred simultaneously. The relationship between the signal against p_x within the high-shear region (circled in black) is shown in Fig. 10(b). The profiles exhibited the parabolic relationship predicted by Eq. (7) for $|p_x| < 100$ s mm^{-1}. It is noteworthy that the product of the signals for cases 1 and 2 is equal to the signal from case 3, as was observed from the test cases in the preceding section. This relation confirms that the velocity distributions are sufficiently independent for Eq. (12) to be valid.

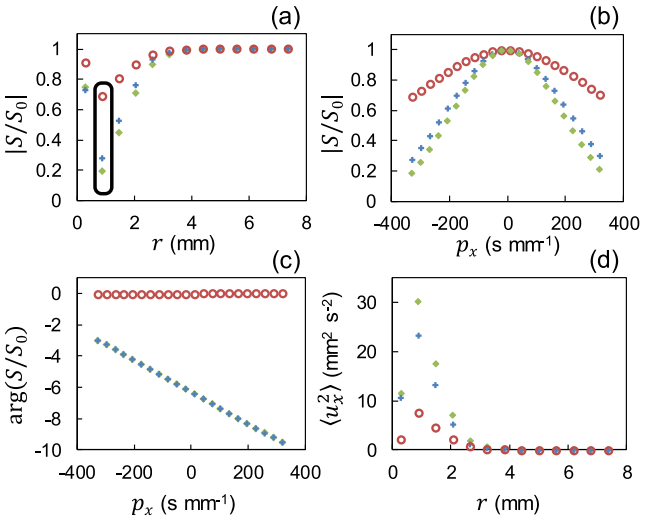

Fig. 10. Analysis of granular Couette flow of 0.44 mm particles with e_n = 0.9, μ_f = 0.1, and U = 17 mm s^{-1} using MRI simulation method. (a) Normalised absolute signal across the gap (p_x = 330 s mm^{-1}). (b) Normalised absolute signal against p_x for the region circled in black on (a). (c) Angle of the complex signals against p, the local mean velocity is given by the gradient. (d) Velocity variance profile. Considering only particle translation (case 1) (+); Considering only particle rotation (case 2) (○); Considering both rotation and translation (case 3) (♦).

Fig. 10(c) shows the angle of the complex signal against p_x for the high shear region. The local mean velocity was found from the gradient of these data. The profiles from cases 1 and 3 were similar, while case 2 had a gradient close to zero. These data were consistent with the theoretical model prediction that the rotation component was real. Thus, rotation has no effect on measurement of mean translational velocity and the model for the signal ignoring rotation given by Eq. (7) is suitable for mean velocity measurements.

The local variance of the velocity in the sample was found by fitting Eq. (7) to the absolute value of the complex simulated MRI signals such as those shown in Fig. 10(b). The resulting velocity variance across the gap is shown in Fig. 10(d). The variance profile mirrors the signal profile, where regions with large velocity fluctuations corresponded to high signal attenuation. The variance obtained by only considering translational motion (case 1) was about 75% of the variance measured when including both modes of motion (case 3). This disparity demonstrates that the velocity

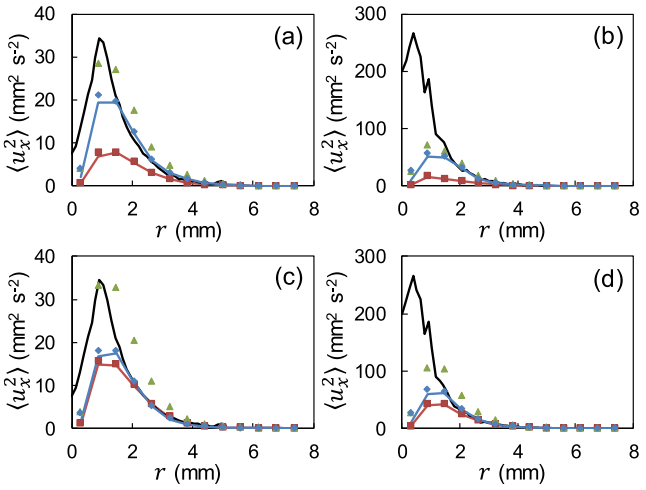

Fig. 12. Comparison of experimental and simulated velocity variance profiles of Couette shear with 0.60 mm d_p particles. The MRI experiments (▬) were reported previously [22] and were run at the same U as the simulations.DEM simulations were performed with parameters of (a) $\mu_f = 0.1$, U = 17 mm s^{-1}, (b) $\mu_f = 0.1$, U = 41 mm s^{-1}, (c) $\mu_f = 0.5$, U = 17 mm s^{-1}, (d) $\mu_f = 0.5$, U = 41 mm s^{-1}. MRI simulations incorporated translational motion only (case 1) (♦), angular motion only (case 2) (■), and both translational and angular motion (case 3) (▲). Direct averages were calculated for the translational velocity variance (▬) and angular velocity variance (▬).

variance measured by MRI is not a direct measurement of translational velocity fluctuations; instead it is amplified due to the additional signal attenuation induced by rotating granules.

Figs. 11 and 12 show the velocity variance profiles recovered by fitting Eq. (13) to the simulated MRI signal from the annular shear DEM simulations for 0.44 mm and 0.60 mm diameter particles. In these simulations, the apparent velocity variance from granule rotation was a significant fraction of the total variance. In general, the angular motion was 20% of the total variance at the inner wall, this ratio increased with distance across the gap. For $\mu_f = 0.1$, the maximum ratio was about 40% at the outer wall. For $\mu_f = 0.5$, the maximum ratio increased to about 70%. If the friction coefficient is increased, then the torque on a particle increases, increasing its angular velocity. As a result, the sample may have a wider range of angular velocities, increasing the angular velocity variance. The granule radius did not affect the ratio significantly since the increase of the contribution to the signal associated with increasing the radius was counteracted by the 0.44 mm particles experiencing higher angular velocity variances. This finding is consistent with that of Nichol and Daniels [48] where the partition of kinetic energy between translational and rotational modes was found to be insensitive to particle size.

Also shown in Figs. 11 and 12 are the experimental data reported in [22]. For the 17 mm s^{-1} cases, translational motion alone was sufficient to account for the experimentally observed velocity variance for the 0.44 mm particles (Fig. 11a), while rotational motion was required for the 0.60 mm particles (Fig. 12a). Modelling the effect of rotation caused the MRI simulation data to exceed the experiment by up to 50% at the peak value for the 0.44 mm particles. For the 41 mm s^{-1} cases, the MRI simulations with the 0.44 mm diameter particles were in good agreement with the MRI experiments, while those with the 0.60 mm diameter particles showed that the simulated peak variance was less than half that of the experiment, although the decay beyond 1.5 mm was captured accurately. One possible explanation for the discrepancies between the simulation and experiment that are observed in Figs. 11 and 12 is that the rotational velocities about the y and z axes are correlated, i.e. our theoretical model could be flawed in the Couette system. To test this possibility, the apparent velocity variance arising from rotation obtained by direct averaging is shown in Figs. 11 and 12. Compared to the variance fitted to the MRI simulations, the agreement is excellent, indicating that there is no evidence of correlation between rotation velocities about the y and z axes and that MRI can accurately measure the angular velocity variance of granular flows. Therefore, the discrepancy between the simulations and experiment seen here is not due to an error in Eq. (12), instead it may be due to the contact model in DEM being insufficient in this system.

One effect not considered in the contact model used in the DEM simulations is rolling friction. Rotational motion between contacting granules is resisted by frictional torque. This frictional torque, commonly known as "rolling friction" is an important mode of kinetic energy dissipation and provides support to geometrically stable granular structures [49]. Rolling friction has been found to have a minimal effect on the translational velocity distribution of sheared granular flows in the intermediate regime [50]. Here additional simulations were run including rolling friction to test the effect on rotational velocity distributions. Fig. 13 shows the velocity variance profiles across the gap for rolling friction coefficients of 0, 0.05, and 0.5. Typical values for the rolling friction are around 0.05. The results indicate that rolling friction inhibits granule rotation, thus reducing the angular velocity variance. Including rolling friction in the DEM simulations may explain the discrepancy seen for the 0.44 mm diameter particles in Fig. 11. It is recommended that future experiments include measurements of the static and rolling friction coefficients to ensure the validity of the contact model used in DEM.

Rolling friction is not sufficient to explain the discrepancy seen for the 0.60 mm diameter particles in Fig. 12. It is hypothesised that the experimental velocity variance in [22] may exceed that seen in the simulations owing to an effect related to the particles attached to the walls, however further work is required to investigate this effect in more detail.

The significant contribution that rotation makes to the velocity variance fitted from the MRI signal raises an important consideration when validating DEM simulations of velocity distributions against MRI experiments. Unlike particle tracking methods, which measure the translational velocity variance, the MRI velocity variance consists of both translational and angular variances. Thus, it is necessary to analyse the DEM simulation data in accordance with the physics of MRI signal acquisition. The results shown here confirm that in most cases the best agreement with MRI experiments is achieved by incorporating the effects of both translational and rotational motion into the analysis of DEM simulation data.

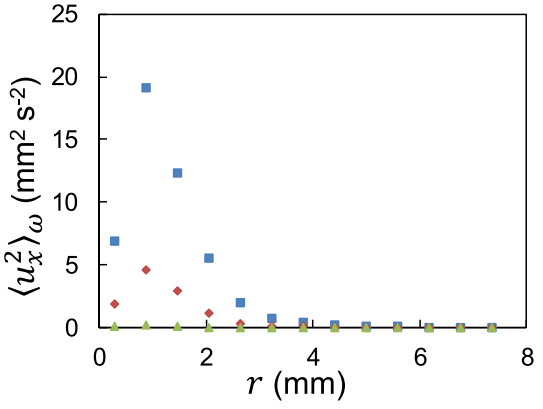

Fig. 13. DEM average angular velocity variance across annular gap for d_p = 0.44 mm, $\mu_f = 0.1$, $U = 41$ mm s^{-1} for rolling friction coefficient, $\mu_r = 0$ (■), 0.05 (♦), 0.5 (▲).

The results also demonstrate that rotational motion can influence the behaviour of the system. The simulations with different particles and rotational speeds show inconsistent partitioning of energy between the rotational and translational motion. Accurate contact models, and possibly boundary conditions, are required in order to describe this partitioning effectively. Therefore, to fully validate DEM it is critical to obtain measurements of mean velocity, velocity fluctuations, and the fluctuations arising from rotational motion. This work presents a first attempt to probe the rotational motion of granular flows using MRI. The analysis shows that PFG MRI is sensitive to both rotational and translational motion. The effects of rotational and translational motion are multiplicative. Therefore, if an independent measurement of translational motion were performed, the rotational component of the signal (and hence the angular velocity variance) could be obtained from the total signal.

5. Conclusions

A theoretical model describing the MRI signal in terms of the translational and angular velocity distributions of granules was developed, shown by Eq. (12). Soft-sphere DEM simulations were conducted for a collection of spherical particles under annular shear flow. The mean and variance of the translational velocity were calculated by two approaches. (1) A direct averaging method as justified in the supplementary material. (2) Fitting the truncated signal model to a simulated MRI signal acquired from the DEM particle trajectories. Simulated MRI allowed for inclusion and exclusion of particle rotation. For an idealised test case of a non-interacting particles, the theoretical model perfectly describes the behaviour of the signal for $p_x < 330\ \mathrm{mm\ s^{-1}}$. For annular shear flow, fitting Eq. (13) to simulated MRI data at low p_x returned velocity variances that were within the standard error of the variances of directly averaged velocity data. These simulations show that when using experimental MRI data to validate simulations, particle rotation must be considered.

The theoretical model of the signal considering granule rotation developed here has the potential to enable experimental MRI measurements of the angular velocity distribution. Few other techniques are sensitive to granular rotation. This model shows that the rotational and translational contributions to the signal are multiplicative. Hence if an independent measure of translational motion is possible, the rotational motion can also be determined. This information would allow for valuable insights into the dynamics of flowing granular media, and is the subject of ongoing work.

Appendix A

The exponentials within the volume integral of Eq. (11) are expressed as Taylor series expansions:

$$S(p_x) = \frac{\exp(ip_x v_x)\exp\left(-\frac{p_x^2}{2}\langle u_x^2\rangle\right)}{\sqrt{\langle u_x^2\rangle 2\pi}} \times \int P(\omega_y)\int P(\omega_z) \times \iiint_V \sum_{n=0}^{\infty}\frac{i^n(p_x z\omega_y)^n}{n!}\sum_{n=0}^{\infty}\frac{i^n(p_x y\omega_z)^n}{n!}\,dV_p d\omega_y d\omega_z. \tag{23}$$

Expressing these series multiplications as Cauchy products gives:

$$S(p_x) = \frac{\exp(ip_x v_x)\exp\left(-\frac{p_x^2}{2}\langle u_x^2\rangle\right)}{\sqrt{\langle u_x^2\rangle 2\pi}} \times \int P(\omega_y)\int P(\omega_z) \times \iiint_V \sum_{m=0}^{\infty}\sum_{l=0}^{m}\frac{i^m p_x^m z^l \omega_y^l y^{m-l}\omega_z^{m-l}}{l!(m-l)!}\,dV_p d\omega_y d\omega_z. \tag{24}$$

Taking the independent terms out of the volume integral gives:

$$S(p_x) = \frac{\exp(ip_x v_x)\exp\left(-\frac{p_x^2}{2}\langle u_x^2\rangle\right)}{\sqrt{\langle u_x^2\rangle 2\pi}} \times \sum_{m=0}^{\infty}\sum_{l=0}^{m}\frac{i^m p_x^m}{l!(m-l)!} \times \int P(\omega_y)\omega_y^l \int P(\omega_z)\omega_z^{m-l}\iiint_V z^l y^{m-l}\,dV_p d\omega_y d\omega_z. \tag{25}$$

The triple integral over the spherical region was found by converting to spherical coordinates and performing iterated integrals using reduction formulae. The volume integral in Eq. (25) was expressed as $\int x^a y^b dV$, where $a = m - l$ and $b = l$ are positive integers. This integral was converted into spherical coordinates:

$$\int_0^r\int_0^{\pi}\int_0^{2\pi} r^{a+b+2}\sin(\theta)^{a+b+1}\sin(\varphi)^a\cos(\varphi)^b\,d\varphi d\theta dr \tag{26}$$

The integral with respect to φ was found using the following reduction formula which was applied recursively:

$$I_{a,b} = \int \sin^a(x)\cos^b(x)dx = \frac{\sin^{a-1}(x)\cos^{b+1}(x)}{a+b} + \frac{a-1}{a+b}I_{a-2,b} \tag{27}$$

As the definite integral is evaluated over the limits 0 and 2π, the first term on the right-hand side of Eq. (27) is zero for every recursion due to the presence of the sine function. If a is an even integer, then the final term in the series is $I_{0,b} = \int \cos^b(x)$. If a is an odd integer, then the final recursion $I_{1,b}$ contains a sine term and hence is zero. From this point onwards, we let a be an even integer. The coefficient of $I_{0,b}$ is the product of the preceding recursions.

$$I_{a,b} = I_{0,b}\prod_{i=1}^{a/2}\frac{2i-1}{2i+b} \tag{28}$$

The following recursion formula is used to derive $I_{0,b}$:

$$I_b = \int \cos^b(x)dx = \frac{\sin(x)\cos^{b-1}(x) + (b-1)I_{b-2}}{b} \tag{29}$$

Taking the definite integral over 0 to 2π cancels out all the trigonometric terms. If b is an even integer, then the final recursion $I_0 = \int_0^{2\pi} dx = 2\pi$. Thus, we let b be an even integer. I_0 has a coefficient that is the product of the preceding recursions, thus:

$$I_{a,b} = 2\pi\prod_{j=1}^{b/2}\frac{2j-1}{2j}\prod_{i=1}^{a/2}\frac{2i-1}{2i+b} \tag{30}$$

The integral with respect to θ was obtained by the following reduction formula:

$$I_c = \int \sin^c(x)dx = \frac{\cos(x)\sin^{c-1}(x) + (c-1)I_{c-2}}{c} \tag{31}$$

where $c = a + b + 1$. If a and b are even, then c is odd. For this integral, the limits are 0 and π, hence the first term in Eq. (31) is zero due to the sine function. The final term in the recursion is $I_1 = \int_0^{\pi}\sin(x)dx = 2$. The coefficient of I_1 is the product of preceding coefficients, thus:

$$I_c = 2\prod_{k=1}^{(c-1)/2}\frac{2k}{2k+1} \tag{32}$$

Integration with respect to r from 0 to R gives:

$$\int_0^R r^{a+b+2}dr = \frac{R^{a+b+3}}{a+b+3} \tag{33}$$

The product of Eq. (30), (32), and (33) gives the spherical integral for Eq. (26):

$$\int x^a y^b dV = \frac{4\pi R^{a+b+3}}{a+b+3} \prod_{k=1}^{(c-1)/2} \frac{2k}{2k+1} \prod_{j=1}^{b/2} \frac{2j-1}{2j} \prod_{i=1}^{a/2} \frac{2i-1}{2i+b} \tag{34}$$

This integral is expressed as $c_{a,b}R^{a+b+3}$, the product of the granule radius term and a coefficient $c_{a,b}$, which is equal to:

$$c_{a,b} = \frac{4\pi}{a+b+3} \prod_{k=1}^{(c-1)/2} \frac{2k}{2k+1} \prod_{j=1}^{b/2} \frac{2j-1}{2j} \prod_{i=1}^{a/2} \frac{2i-1}{2i+b}. \tag{35}$$

If either one or both exponents are odd, the integral is equal to zero. Hence the signal associated with particle rotation is real. If the exponents are even, then the result takes the form: $c_{l,m-l}R^{m+3}$, where R is the particle radius and $c_{l,m-l}$ is the coefficient obtained from the triple integral for a particular term in the series.

Eq. (25) is then integrated with respect to each of the angular velocity components, these integrals take the following form:

$$\int_{-\infty}^{+\infty} \frac{1}{\sqrt{2\pi\langle\omega_y^2\rangle}} \exp\left(-\frac{\omega_y^2}{2\langle\omega_y^2\rangle}\right) \omega_y^l d\omega_y = \frac{(l-1)!!\sqrt{\pi}\left(2\langle\omega_y^2\rangle\right)^{(l+1)/2}}{2^{l/2}\sqrt{2\pi\langle\omega_y^2\rangle}} = (l-1)!!\langle\omega_y^2\rangle^{l/2}. \tag{36}$$

Substituting Eq. (34) and (36) into Eq. (25) gives the result shown in Eq. (12).

Acknowledgements

The author(s) wish to acknowledge the use of New Zealand eScience Infrastructure (NeSI) high performance computing facilities, consulting support and/or training services as part of this research. New Zealand's national facilities are provided by NeSI and funded jointly by NeSI's collaborator institutions and through the Ministry of Business, Innovation & Employment's Research Infrastructure programme. URL https://www.nesi.org.nz.

The authors would also like to thank the Royal Society of New Zealand (contract MAU1712) and the University of Canterbury Doctoral Scholarships for financial support.

Appendix B. Supplementary material

Supplementary data to this article can be found online at https://doi.org/10.1016/j.jmr.2019.106569.

References

[1] P. Jop, Y. Forterre, O. Pouliquen, A constitutive law for dense granular flows, Nature 441 (2006) 727–730.
[2] K. Kamrin, G. Koval, Nonlocal constitutive relation for steady granular flow, Phys. Rev. Lett. 108 (2012) 178301.
[3] C.K.K. Lun, S.B. Savage, D.J. Jeffrey, N. Chepurniy, Kinetic theories for granular flow: inelastic particles in Couette flow and slightly inelastic particles in a general flowfield, J. Fluid Mech. 140 (1984), 223 223.
[4] Q. Zhang, K. Kamrin, Microscopic description of the granular fluidity field in nonlocal flow modeling, Phys. Rev. Lett. 118 (2017) 058001.
[5] R. Artoni, P. Richard, Effective wall friction in wall-bounded 3D dense granular flows, Phys. Rev. Lett. 115 (2015) 158001.
[6] C.K.K. Lun, Kinetic theory for granular flow of dense, slightly inelastic, slightly rough spheres, J. Fluid Mech. 233 (1991) 539–559.
[7] J.T. Jenkins, C. Zhang, Kinetic theory for identical, frictional, nearly elastic spheres, Phys. Fluids 14 (2002) 1228–1235.
[8] G.D. Cody, D.J. Goldfarb, G.V. Storch Jr, A.N. Norris, Particle granular temperature in gas fluidized beds, Powder Technol. 87 (1996) 211–232.
[9] W. Dijkhuizen, G.A. Bokkers, N.G. Deen, M. Van Sint Annaland, J.A.M. Kuipers, Extension of PIV for measuring granular temperature field in dense fluidized beds, AlChE J. 53 (2007) 108–118.
[10] N. Menon, D.J. Durian, Diffusing-wave spectroscopy of dynamics in a three-dimensional granular flow, Science 275 (1997) 1920–1922.
[11] P. Dixon, D.J. Durian, Speckle visibility spectroscopy and variable granular fluidization, Phys. Rev. Lett. 90 (2003) 184302.
[12] R.D. Wildman, C.M. Hrenya, J.M. Huntley, T. Leadbeater, D.J. Parker, Experimental determination of temperature profiles in a sheared granular bed containing two and three sizes of particles, Granular Matter. 14 (2012) 215–220.
[13] R. Wildman, J. Huntley, D. Parker, Granular temperature profiles in three-dimensional vibrofluidized granular beds, Phys. Rev. E 63 (2001) 061311.
[14] G. Mohs, O. Gryczka, S. Heinrich, L. Mörl, Magnetic monitoring of a single particle in a prismatic spouted bed, Chem. Eng. Sci. 64 (2009) 4811–4825.
[15] K.A. Buist, A.C. van der Gaag, N.G. Deen, J.A.M. Kuipers, Improved magnetic particle tracking technique in dense gas fluidized beds, AlChE J. 60 (2014) 3133–3142.
[16] J.D. Seymour, A. Caprihan, S.A. Altobelli, E. Fukushima, Pulsed gradient spin echo nuclear magnetic resonance imaging of diffusion in granular flow, Phys. Rev. Lett. 84 (2000) 266–269.
[17] M. Nakagawa, S.A. Altobelli, A. Caprihan, E. Fukushima, E.K. Jeong, Non-invasive measurements of granular flows by magnetic resonance imaging, Exp. Fluids 16 (1993) 54–60.
[18] D.J. Holland, C.R. Müller, J.S. Dennis, L.F. Gladden, A.J. Sederman, Spatially resolved measurement of anisotropic granular temperature in gas-fluidized beds, Powder Technol. 182 (2008) 171–181.
[19] X. Yang, C. Huan, D. Candela, R. Mair, R. Walsworth, Measurements of grain motion in a dense, three-dimensional granular fluid, Phys. Rev. Lett. 88 (2002) 044301.
[20] R. Savelsberg, D.E. Demco, B. Blümich, S. Stapf, Particle motion in gas-fluidized granular systems by pulsed-field gradient nuclear magnetic resonance, Phys. Rev. E 65 (2002) 020301.
[21] D.M. Mueth, G.F. Debregeas, G.S. Karczmar, P.J. Eng, S.R. Nagel, H.M. Jaeger, Signatures of granular microstructure in dense shear flows, Nature 406 (2000) 385–389.
[22] H.T. Fabich, T.I. Brox, D. Clarke, J.D. Seymour, S.L. Codd, P. Galvosas, J. Brown, A. J. Sederman, D.J. Holland, Measurements of the velocity distribution for granular flow in a Couette cell, Phys. Rev. E 98 (2018) 062901.
[23] J. Bittoun, J. Taquin, M. Sauzade, A computer algorithm for the simulation of any Nuclear Magnetic Resonance (NMR) imaging method, Magn. Reson. Imaging 2 (1984) 113–120.
[24] K. Jurczuk, M. Kretowski, J.J. Bellanger, P.A. Eliat, H. Saint-Jalmes, J. Bézy-Wendling, Computational modeling of MR flow imaging by the lattice Boltzmann method and Bloch equation, Magn. Reson. Imaging 31 (2013) 1163–1173.
[25] P.A. Cundall, O.D.L. Strack, A discrete numerical model for granular assemblies, Géotechnique 29 (1979) 47–65.
[26] S. Schöllmann, Simulation of a two-dimensional shear cell, Phys. Rev. E – Statist. Phys., Plasmas, Fluids, Related Interdisciplinary Topics 59 (1999) 889–899.
[27] G.J. Finnie, N.P. Kruyt, M. Ye, C. Zeilstra, J.A.M. Kuipers, Longitudinal and transverse mixing in rotary kilns: A discrete element method approach, Chem. Eng. Sci. 60 (2005) 4083–4091.
[28] H. Komossa, S. Wirtz, V. Scherer, F. Herz, E. Specht, Transversal bed motion in rotating drums using spherical particles: Comparison of experiments with DEM simulations, Powder Technol. 264 (2014) 96–104.
[29] P.A. Langston, U. Tüzün, D.M. Heyes, Discrete element simulation of granular flow in 2D and 3D hoppers: Dependence of discharge rate and wall stress on particle interactions, Chem. Eng. Sci. 50 (1995) 967–987.
[30] Y. Forterre, O. Pouliquen, Flows of dense granular media, Ann. Rev. Fluid Mech. 40 (2008) 1–24.
[31] E. Khain, Hydrodynamics of fluid-solid coexistence in dense shear granular flow, Phys. Rev. E 75 (2007) 051310.
[32] K. Saitoh, H. Hayakawa, Rheology of a granular gas under a plane shear, Phys. Rev. E 75 (2007) 021302.
[33] S. Chialvo, S. Sundaresan, A modified kinetic theory for frictional granular flows in dense and dilute regimes, Phys. Fluids 25 (2013) 070603.
[34] Y. Tsuji, T. Kawaguchi, T. Tanaka, Discrete particle simulation of two-dimensional fluidized bed, Powder Technol. 77 (1993) 79–87.
[35] N.G. Deen, M. Van Sint Annaland, M.A. Van der Hoef, J.A.M. Kuipers, Review of discrete particle modeling of fluidized beds, Chem. Eng. Sci. 62 (2007) 28–44.
[36] C.R. Müller, D.J. Holland, A.J. Sederman, S.A. Scott, J.S. Dennis, L.F. Gladden, Granular temperature: Comparison of Magnetic Resonance measurements with Discrete Element Model simulations, Powder Technol. 184 (2008) 241–253.
[37] C.R. Müller, S.A. Scott, D.J. Holland, B.C. Clarke, A.J. Sederman, J.S. Dennis, L.F. Gladden, Validation of a discrete element model using magnetic resonance measurements, Particuology 7 (2009) 297–306.
[38] C.M. Boyce, D.J. Holland, S.A. Scott, J.S. Dennis, Adapting data processing to compare model and experiment accurately: A discrete element model and magnetic resonance measurements of a 3d cylindrical fluidized bed, Ind. Eng. Chem. Res. 52 (2013) 18085–18094.
[39] E. Fukushima, Nuclear magnetic resonance as a tool to study flow, Ann. Rev. Fluid Mech. 31 (1999) 95–123.
[40] C.A. Wheeler-Kingshott, Y. Crémillieux, S.J. Doran, Burst imaging: rotation artifacts and how to correct them, J. Magn. Reson. 143 (2000) 161–171.
[41] S. Kuczera, P. Galvosas, Advances and artefact suppression in RARE-velocimetry for flow with curved streamlines, J. Magn. Reson. 259 (2015) 135–145.
[42] C. Kloss, C. Goniva, A. Hager, S. Amberger, S. Pirker, Models, algorithms and validation for opensource DEM and CFD-DEM, Prog. Comput. Fluid Dyn. 12 (2012) 140–152.

[43] M. Rackl, K.J. Hanley, A methodical calibration procedure for discrete element models, Powder Technol. 307 (2017) 73–83.
[44] H. Khawaja, S. Scott, M. Virk, M. Moatamedi, Quantitative analysis of accuracy of voidage computations in CFD-DEM simulations, J. Comput. Multiphase Flows 4 (2012) 183–192.
[45] D.A. Clarke, A.J. Sederman, L.F. Gladden, D.J. Holland, Investigation of void fraction schemes for use with CFD-DEM simulations of fluidized beds, Ind. Eng. Chem. Res. 57 (2018) 3002–3013.
[46] U.M. Scheven, J.P. Crawshaw, V.J. Anderson, R. Harris, M.L. Johns, L.F. Gladden, A cumulant analysis for non-Gaussian displacement distributions in Newtonian and non-Newtonian flows through porous media, Magn. Reson. Imaging 25 (2007) 513–516.
[47] C.R. Rao, Linear Statistical Inference and Its Applications, Wiley, New York, 1973.
[48] K. Nichol, K.E. Daniels, Equipartition of rotational and translational energy in a dense granular gas, Phys. Rev. Lett. 108 (2012) 018001.
[49] J. Ai, J.F. Chen, J.M. Rotter, J.Y. Ooi, Assessment of rolling resistance models in discrete element simulations, Powder Technol. 206 (2011) 269–282.
[50] X. Wang, H.P. Zhu, A.B. Yu, Microdynamic analysis of solid flow in a shear cell, Granular Matter. 14 (2012) 411–421.